

1 **Estimating the impact of a major hurricane on**
2 **transport processes**

3 Thomas Dobbelaere, Emmanuel Hanert

4 March 5, 2021

5 **Abstract**

6 In most hydrodynamic model studies, currents and waves are simu-
7 lated separately. This is especially true for the simulation of passive
8 drifters, whose trajectories are often computed based solely on cur-
9 rents. Although this simplification holds for most situations, as the force
10 exerted by waves on currents can be neglected in fair weather condi-
11 tions, it may lead to significant errors during storm conditions, when
12 currents are strongly influenced by wind-generated waves. In this study,
13 we investigate current-wave interactions in heavy-wind conditions by
14 coupling the unstructured-mesh hydrodynamic model SLIM with the
15 wave model SWAN. We apply the coupled model in the Florida Reef
16 Tract during Hurricane Irma (Sep. 2017) and show that it successfully
17 reproduces both the observed wave behavior and storm surge during
18 the hurricane. The modeled currents are then used to simulate the
19 trajectories of passive drifters during the passage of the hurricane. Our
20 results show that taking wave force into account induces variations of
21 up 1 m/s in modelled currents on the continental shelf break as well
22 as in the vicinity of reefs and islands. Wave-current interactions can
23 therefore deflect the trajectories of drifting material by up to 10 km on
24 the passage of the storm **Add something?**. These results strongly advo-
25 cate for the inclusion of wave forces while studying transport processes
26 (sediments, pollutants, larvae, etc.) in heavy-wind conditions.

27 **1 Introduction**

28 Wave-current interactions in coastal areas are of great importance for coastal
29 engineering as they play a key role in sediment transport, morphological
30 evolution and pollutant mixing (Bever and MacWilliams, 2013; Li and Johns,
31 1998). However, these interactions are highly nonlinear and can vary sig-
32 nificantly in space and time (Wu et al., 2011). Wave-induced currents are
33 generated by wave radiation gradients (Longuet-Higgins, 1970), affecting
34 water levels near shorelines and wave breaking points (Longuet-Higgins
35 and Stewart, 1964), while changes in water levels and currents, in turn,
36 affect the motion and evolution of the waves (Sikirić et al., 2013). Cou-
37 pled wave-current models are therefore required to capture these complex
38 interactions.

39 As coastal oceans are characterized by complex topology with islands,
40 inlets and estuaries, unstructured (usually two-dimensional) models are pre-
41 ferred as structured grid models show limitations in resolving topologically-
42 controlled nearshore processes (Wu et al., 2011; Chen et al., 2007). The
43 effect of wave-interactions becomes even more significant in the case of hur-
44 rricanes, that generate large wind-waves and disturb ocean conditions (Liu
45 et al., 2020) by causing coastal upwellings on continental shelves (Smith,
46 1982) and inducing strong currents, waves and storm surges in nearshore
47 and coastal regions (Dietrich et al., 2010; Weisberg and Zheng, 2006).

48 South Florida and the Gulf of Mexico are particularly vulnerable to hurricanes
49 (Malmstadt et al., 2009) and modelling studies predict tropical cyclones to
50 increase both in frequency and intensity in this region (Marsooli et al.,
51 2019; Knutson et al., 2010). Being able to accurately model wave-current
52 interactions in this area becomes thus critical. *Expand...*

53 Individual-based modelling of particulates has been extensively used to
54 study the transport of drifting materials such as pollutants, sediments or
55 larvae (Garcia-Pineda et al., 2020; Liubartseva et al., 2018; Figueiredo et al.,
56 2013; Frys et al., 2020). Although some of these studies take the impact
57 of waves into account by adding a Stokes drift velocity, *i.e.* the net drift of a
58 floating particle in the direction of the wave propagation (Van Den Bremer
59 and Breivik, 2018), to the Eulerian currents, they usually neglect the wave-
60 induced currents. Such practice is reasonable in the case of fair weather,

61 when wave-induced forces exerted on currents are relatively smaller, but
62 might lead to significant inaccuracies during storm conditions. To assess
63 the importance of wave-current interactions during a tropical cyclone, we
64 investigated the transport of drifting particulates on the Florida shelf during
65 Hurricane Irma, one of the strongest and costliest tropical cyclones on
66 records in the Atlantic Basin (Chen et al., 2007), that made landfall in Florida
67 in September 2017.

68 In this study, we developed an unstructured coupled wave-current model of
69 South Florida to simulate the ocean circulation during hurricane Irma. Both
70 modelled currents and waves were validated against field measurements
71 and were then used to simulate the transport of drifting material in the
72 Florida Keys and the Florida inner shelf during the storm. Model outputs
73 were then compared with uncoupled simulation results in order to assess
74 the impact of wave-induced forces and Stokes drift on the modelled currents
75 and transports.

76 **2 Methods**

77 **2.1 Study area and observational data**

78 Large-scale ocean circulation around South Florida is dominated by the
79 Florida Current (FC), which originates from the Loop Currents (LC) where it
80 enters the Florida Straits from the Gulf of Mexico, and, downstream, forms
81 the Gulf Stream. The FC is a major western boundary current character-
82 ized by spatial variability and meandering, associated with the presence
83 of cyclonic eddies between the core of the current and the complex reef
84 topography of the Florida Reef Tract (FRT) (Lee et al., 1995; Kourafalou and
85 Kang, 2012). The northern half of these reefs are made of early Holocene
86 reef frameworks and indurated sand ridges while the southern part (the
87 Florida Keys) is composed of a chain of limestone islands, fossilized rem-
88 nants of ancient coral reefs and sand bars (Hoffmeister and Multer, 1968;
89 Shinn, 1988; Lidz and Shinn, 1991). The variability of the FC extends over
90 a large range of spatial and temporal scales, with periods of 30-70 days in
91 the Lower Keys (Lee et al., 1995) and shorter periods of 2-21 days in the
92 Upper Keys (Lee and Mayer, 1977), and exhibits significant seasonal and

93 interannual cycles (Johns and Schott, 1987; Lee and Williams, 1988; Schott
94 et al., 1988). Circulation on the West Florida Shelf (WFS) on the other hand
95 is forced by local winds and tidal fluctuations (Lee and Smith, 2002; Liu and
96 Weisberg, 2012).

97 The state of the ocean around Florida is monitored by an extensive array
98 of tide gauges, current meters and buoys. In this study, we used sea
99 surface elevation measurements from the National Oceanic and Atmospheric
100 Administrations (NOAA) Tides and Currents dataset. These measurements
101 were taken at four locations: two in the Florida Keys (Key West and Vaca
102 Key); one on the eastern coast of Florida (Key West); and one on the western
103 coast (Naples). For the currents, we used ADCP measurements from
104 the University of South Florida's College of Marine Science's (USF/CMS)
105 Coastal Ocean Monitoring and Prediction System (COMPS) for the WFS
106 (Weisberg et al., 2009). More specifically, we used measurements from
107 moorings C10, C12 and C13, respectively located at the 25, 50, and 50
108 m isobaths of the WFS (Liu et al., 2020). Finally, for the waves, we used
109 measurements from four buoys of the NOAA's National Data Buoy Center
110 (NDBC). Two on Florida's Eastern shelf and two on the WFS. The locations
111 of all measurement stations are shown on Fig. 1

112 **2.2 Wind and atmospheric pressure during Hurricane Irma**

113 Irma made landfall in Florida on 10 September 2017 as a category 3 storm,
114 first at Cudjoe Key (Florida Keys) and later on Marco Island, south to Naples
115 (see hurricane track in Fig. 1). It then weakened to a category 2 storm as it
116 moved further inland (Pinelli et al., 2018). The storm caused damages to
117 up to 75% of the buildings at his landfall point in the Florida Keys, making it
118 one of the strongest and costliest hurricanes on record in the Atlantic basin
119 (Xian et al., 2018; Zhang et al., 2019). The strongest reported wind speed
120 was 50 m/s on Marco Island while the highest recorded storm surge was
121 2.3 m, although larger wind speed likely occurred in the Florida Keys (Pinelli
122 et al., 2018) In order to reproduce the wind profile of Irma in our model,
123 we used high-resolution H*Wind wind fields (Powell et al., 1998). As these
124 data represent 1-min averaged wind speeds, we multiplied them by a factor
125 0.93 to obtain 10-min averaged wind speeds (Harper et al., 2010), which

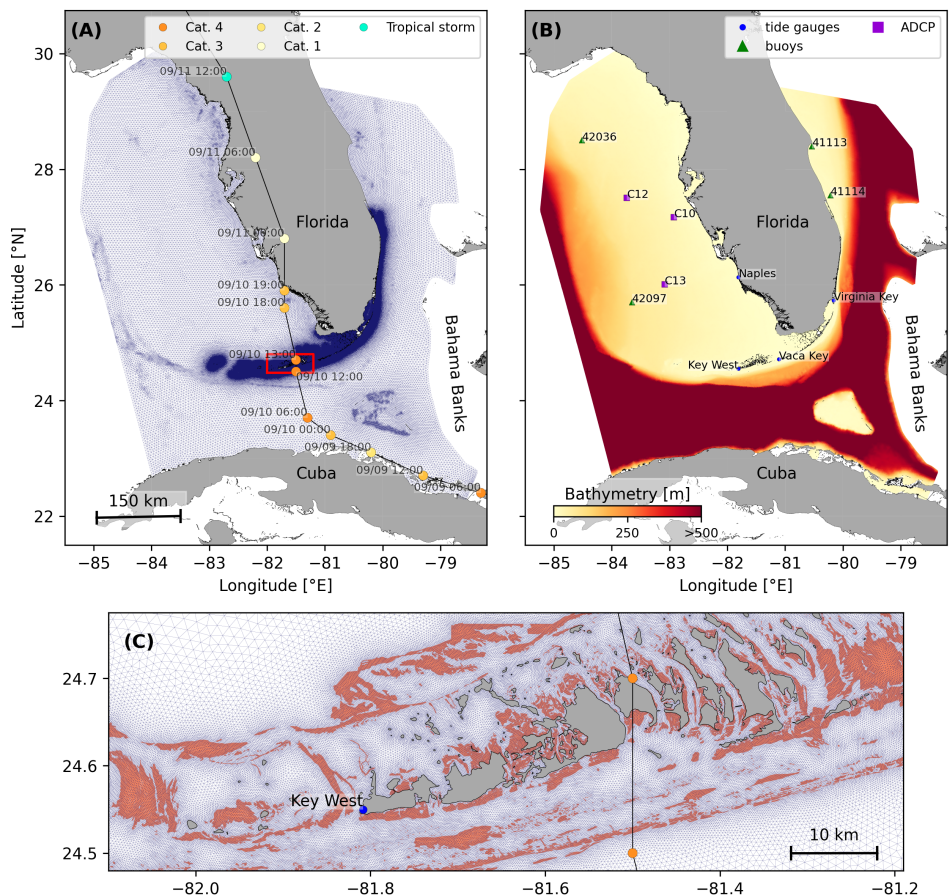


Fig. 1: **A:** Mesh of the computational domain with the trajectory of Irma, category of the hurricane is given by the Saffir-Simpson color scale. **B:** Bathymetry of the domain with the location of stations used for the validation of the model outputs. **C:** Close up view of the Lower Keys area, where the mesh resolution reaches 100m near reefs (shown in coral) and islands (highlighted in dark grey) *Improve plot to better see the mesh...*

126 are more consistent with the time step of our model. Furthermore, H*Wind
 127 wind profiles did not cover the whole model extent during the hurricane and
 128 were thus blended within coarser wind field extracted from ECMWF ERA-5
 129 datasets. Pressure fields of Irma were also constructed using ERA-5 data.
 130 However, the coarse resolution of the dataset smooth out the depression at
 131 the center of the hurricane, leading to an underestimation of the pressure
 132 gradient in our model. To better capture the central depression of Irma, we
 133 built a hybrid pressure field using the position and the minimal pressure of
 134 the core of the hurricane based on its track as recorded in the HURDAT
 135 2 database (Landsea and Franklin, 2013). Based on this information, the
 136 hybrid pressure field was constructed by combining an idealized Holland
 137 pressure profile (Lin and Chavas, 2012) within the radius of maximum
 138 wind speed of Irma (Knaff et al., 2018) with ERA-5 pressure field. The
 139 transition between from the Holland profile to ERA-5 data outside the radius
 140 of maximum wind speed data was performed using a smooth step function.

141 **2.3 Hydrodynamic model**

142 Ocean currents generated during hurricane Irma around South Florida were
 143 modelled using the 2D barotropic version of the unstructured-mesh coastal
 144 ocean model SLIM¹. The model mesh covers an area similar to the model
 145 extent of Dobbelaere et al. (2020b), that includes the FRT but also the Florida
 146 Strait and part of the Gulf of Mexico (Figure 1). However, this area has
 147 been slightly extended northeastward and westward in order to include the
 148 NOAA-NDBC buoys. Furthermore, in order to withstand potential cell drying
 149 during the hurricane, we solved the conservative shallow water equations
 150 with wetting-drying:

$$\begin{aligned}
 \frac{\partial H}{\partial t} + \nabla \cdot (\mathbf{U}) &= 0, \\
 \frac{\partial \mathbf{U}}{\partial t} + \nabla \cdot \left(\frac{\mathbf{U}\mathbf{U}}{H} \right) &= -f\mathbf{e}_z \times \mathbf{U} + \alpha g H \nabla(H - h) - \frac{1}{\rho} \nabla p_{\text{atm}} + \frac{1}{\rho} \boldsymbol{\tau}_s \quad (1) \\
 &\quad + \nabla \cdot (\nu \nabla \mathbf{U}) - \frac{C_b}{H^2} |\mathbf{U}| \mathbf{U} + \gamma(\mathbf{U}_* - \mathbf{U}),
 \end{aligned}$$

¹<https://www.slim-ocean.be>

151 where H is the water column height and \mathbf{U} is the depth-averaged transport;
 152 f is the Coriolis coefficient; g is the gravitational acceleration; h is the
 153 bathymetry; α is a coefficient stating whether the mesh element is wet
 154 ($\alpha = 1$) or dry ($\alpha = 0$); ν is the viscosity; C_b is the bulk bottom drag
 155 coefficient; ∇p_{atm} is the atmospheric pressure gradient; τ_s is the surface
 156 stress due to wind; and γ is a relaxation coefficient towards a reference
 157 transport \mathbf{U}_* . As in Frys et al. (2020) and Dobbelaere et al. (2020b), SLIM
 158 currents were gradually relaxed towards HYCOM (Chassignet et al., 2007) in
 159 regions where the water depth exceeds 50m.

160 At very high wind speeds, the white cap is blown off the crest of the waves,
 161 which generates a layer of droplets that acts as a slip layer for the winds
 162 at the ocean-atmosphere interface (Holthuijsen et al., 2012). This causes
 163 a saturation of the wind drag coefficient for strong winds (Donelan et al.,
 164 2004; Powell et al., 2003). To account for the impact of this saturation
 165 on the surface wind stress in our model, we implemented the wind drag
 166 parameterization of Moon et al. (2007). In this parameterization, the drag
 167 coefficient C_d depends on the wind speed at 10-m height U_{10} according to:

$$C_d = \kappa^2 \log \left(\frac{10}{z_0} \right)^{-2} \quad (2)$$

168 where κ is the von Karman constant. The roughness length z_0 in Eq. (2) is
 169 expressed as:

$$z_0 = \begin{cases} \frac{0.0185}{g} U_*^2 & \text{if } U_{10} \leq 12.5 \text{ m/s ,} \\ [0.085(-0.56U_*^2 + 20.255U_* + 2.458) - 0.58] \times 10^{-3} & \text{if } U_{10} > 12.5 \text{ m/s ,} \end{cases} \quad (3)$$

170 with U_* the friction velocity. The relation between U_{10} and U_* is given by:

$$U_{10} = -0.56U_*^2 + 20.255U_* + 2.458 . \quad (4)$$

171 The mesh resolution depends on the distance to coastlines and reefs fol-
 172 lowing the approach of Dobbelaere et al. (2020b). The mesh is then further
 173 refined according to bathymetry value and gradient, as suggested in the
 174 SWAN user-guide². Such an approach improves the model efficiency as

²<http://swanmodel.sourceforge.net/unswan/unswan.htm>

175 the mesh resolution is only increased where required by the currents and
176 waves dynamics. The mesh was generated with the seamsh³ Python library,
177 which is based on the the open-source mesh generator GMSH (Geuzaine
178 and Remacle, 2009). It is composed of approximately 7.7×10^5 elements.
179 The coarsest elements, far away from the FRT, has a characteristic length
180 of about 5 km whereas the finest elements have a characteristic length of
181 about 100 m near coastlines and reefs (Fig 1).

182 2.4 Wave model

183 Waves were modelled using the parallel unstructured-mesh version of the
184 Simulating WAves Nearshore (SWAN) model (Booij et al., 1999), one of the
185 most commonly used wave models in coastal areas and inland waters. This
186 model solves the action balance equation (Mei, 1989):

$$\frac{\partial N}{\partial t} + \nabla_{\mathbf{x}} \cdot [(\mathbf{c}_g + \mathbf{u})N] + \frac{\partial}{\partial \theta}[c_\theta N] + \frac{\partial}{\partial \sigma}[c_\sigma N] = \frac{S_{in} + S_{ds} + S_{nl}}{\sigma}, \quad (5)$$

187 where $N = E/\sigma$ is the wave action density; θ is the wave propagation
188 direction; σ is the wave relative frequency; c_g is the wave group velocity,
189 $\mathbf{u} = \mathbf{U}/H$ is SLIM depth-averaged current velocity; c_θ and c_σ are the propa-
190 gation velocities in spectral space due to refraction and shifting in frequency
191 due to variations in depth and currents; and S_{in} , S_{ds} , and S_{nl} respectively
192 represent wave growth by wind, wave decay and nonlinear transfers of
193 wave energy through interactions between triplets and quadruplets. Spectra
194 were discretized with 48 direction bins and 50 frequency bins logarithmically
195 distributed from 0.3 to 2 Hz. Exponential wind growth was parameterized
196 using the formulation of Janssen (1991), while dissipations by whitecapping
197 and bottom dissipations followed the formulations of Komen et al. (1984)
198 and Madsen et al. (1989) respectively. Coefficients for exponential wind
199 growth and whitecapping parameterizations were based on the results of
200 Siadatmousavi et al. (2011), and significantly differ from SWAN's default
201 settings. By default, SWAN implements the wind input formulation of Komen
202 et al. (1984) and the steepness-dependent coefficient governing dissipation
203 by whitecapping is a linear function of the wave number. In this study, this
204 steepness-dependent coefficient is a quadratic function of the wave number,

³<https://pypi.org/project/seamsh/>

as it showed better predictions of the significant wave height in the study of Siadatmousavi et al. (2011). The choice of these formulations was motivated by the appearance of numerical instabilities in the region of the Gulf Stream when using SWAN's default parameter values. Finally, wave boundary conditions were derived from WAVEWATCH III (Tolman et al., 2009) spectral outputs at buoy locations.

Surface waves induce a net drift in the direction of the wave propagation, known as the Stokes drift (Van Den Bremer and Breivik, 2018; Stokes, 1880). This net drift has a significant impact on sediment transport in near shore regions (Hoefel and Elgar, 2003), on the formation of Langmuir cells (Langmuir, 1938; Craik and Leibovich, 1976) as well as on the transport of heat, salt or pollutants such as oil or micro-plastic in the upper ocean layer (McWilliams and Sullivan, 2000; Röhrs et al., 2012; Drivdal et al., 2014). To correctly model the Stokes drift profile in mixed wind-driven sea and swell conditions, the full two-dimensional wave spectrum must be represented by a spectral wave model within a wave-current coupling (Van Den Bremer and Breivik, 2018). In this study, depth-averaged Stokes drift was therefore computed by SWAN using the following formula:

$$\mathbf{u}_s = \int_0^{2\pi} \int_0^{+\infty} \frac{\sigma^3}{h \tanh(2kh)} E(\sigma, \theta) (\cos \theta, \sin \theta) d\sigma d\theta , \quad (6)$$

where k is the norm of the wave vector; h is the water depth; and $E(\sigma, \theta)$ is the wave energy density.

2.5 Coupled model

SLIM and SWAN are coupled so that they run on the same computational core and the same unstructured mesh. SLIM is run first and passes computed wind velocities (\mathbf{U}_{10}), water levels ($\eta = H - h$) and depth-averaged currents ($\mathbf{u} = \mathbf{U}/H$) to SWAN, as well as a roughness length (z_0) for the bottom dissipation formulation of Madsen et al. (1989). This roughness length is computed from SLIM's bulk drag coefficient C_b following the approach of Dietrich et al. (2011) so that both models have consistent bottom dissipation parameterizations. SWAN then utilizes these quantities to compute the wave radiation stress gradient, that is then passed to SLIM as the wave-induced

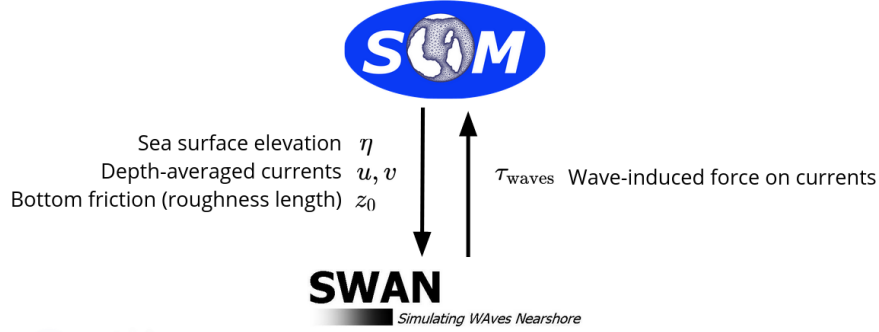


Fig. 2: Schematic illustration of the coupled SLIM+SWAN model.

stress on currents τ_{wave} (Fig. 2). SLIM then uses this quantity to update the value of the surface stress τ_s in Eq. (1), that now becomes the sum of wind and wave-induced stresses $\tau_s = \tau_{\text{wind}} + \tau_{\text{wave}}$.

SLIM's governing equations are integrated using an implicit time integration scheme while SWAN is unconditionally stable (*say that you use the steady version, explain the difference with the unsteady version*) (Dietrich et al., 2010), allowing both models to be run with relatively large time steps. In this study, both models were therefore run sequentially using a time step of 600s, so that each computational core was alternating running either SLIM or SWAN. As in the coupling between SWAN and ADCIRC (Dietrich et al., 2010), both models utilize the same local sub-mesh, allowing for a one-to-one correspondence between the geographic locations of the mesh vertices. No interpolation is therefore needed when passing the discretised variables from one model to the other, which allows an efficient inter-model communication. However, as SLIM applies discontinuous Galerkin finite element methods, an additional conversion step to a continuous framework was required to transmit SLIM nodal quantities to SWAN.

3 Results

We first validated the reconstructed atmospheric fields of hurricane Irma as well the modelled currents and waves of our coupled model against fields measurements. We then use the validated model to simulate the transport of passive drifters in the Lower Keys during the passage of the hurricane.

257 These drifters were advected by two sets of currents: (i) the currents from
258 an uncoupled SLIM simulation of Irma (SLIM) and (ii) the currents modelled
259 by the coupled SLIM+SWAN model (SLIM+SWAN). Furthermore, the depth-
260 averaged Stokes drift was computed using our coupled model (Stokes_C)
261 and an uncoupled SWAN simulation of the hurricane (Stokes_U). We then
262 simulated the trajectories of passive drifters during the passage of the
263 Irma in the Lower Keys using different combinations of these fields. These
264 trajectories were finally compared to evaluate the impact of the wave-current
265 interactions and the Stokes drift on the transport processes during a major
266 hurricane.

267 **3.1 Model validation**

268 H*Wind winds and hybrid pressure field agree well with station measure-
269 ments at Vaca Key station (Fig. 3). The hybrid pressure field shows better
270 agreement with observations than ERA-5 pressure as it successfully re-
271 produces the storm depression. ERA-5 fields, on the other hand, fail to
272 resolve the low pressure at the core of the hurricane due to their coarser
273 grid, leading to an overestimation of 8 mbar of the storm depression. Both
274 H*Wind and ERA-5 agree well with observed wind speeds although both
275 data sets tend to slightly overestimate the width and intensity of the wind
276 peak. However, H*wind profiles show a better match with the timing of the
277 observed peak, as ERA-5 winds tend to anticipate it. H*wind also exhibits a
278 slightly narrower peak in wind speed, which better agrees with observations.
279 Hydrodynamic outputs of the coupled wave-current agree well with tide
280 gauge (Fig. 4) and ADCP measurements (Fig. 5). The timing and amplitude
281 of the storm surges are well reproduced by the coupled model, the largest
282 model error being an overestimation of 18 cm of the elevation peak at
283 Virginia Key. The fit is especially good at Naples, where both the positive
284 and negative surges are captured by the coupled model with an error of less
285 than 5 cm. This result is of interest as negative surges, although less studied,
286 affect water exchanges between the estuaries and the coastal ocean and
287 disturb the benthic ecosystems (Liu et al., 2020). Modelled 2D currents were
288 validated against depth-averaged ADCP measurements at mooring station
289 C10, C12 and C13 (Fig. 5). As in Liu et al. (2020), we performed the vector

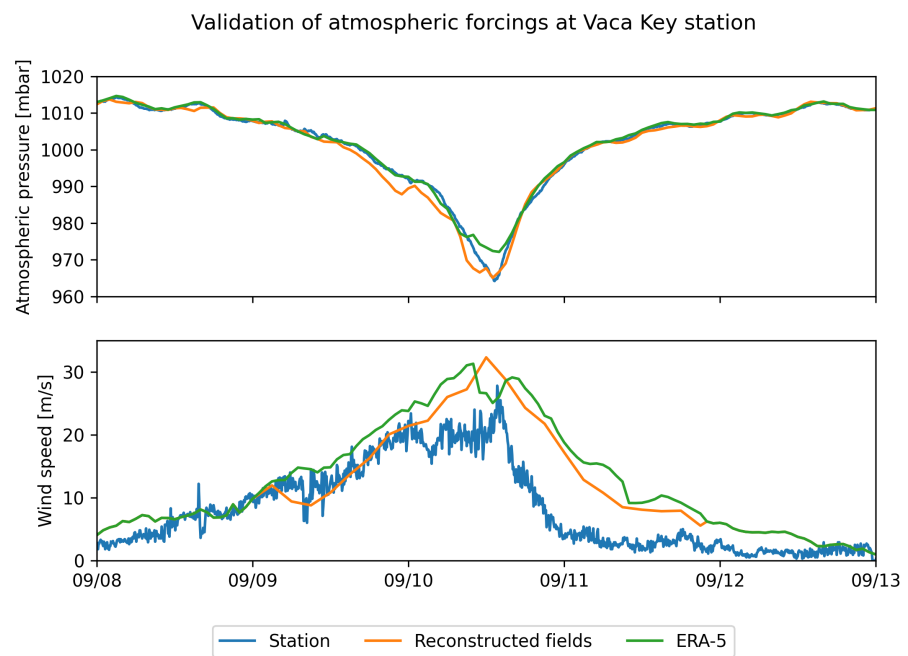


Fig. 3: Comparison of reconstructed wind atmospheric pressure with field measurements and coarser ECMWF ERA-5 profiles at Vaca Key station. The generated hybrid atmospheric forcings better capture the observed storm depression while H*wind winds better match the measured peak in wind speed.

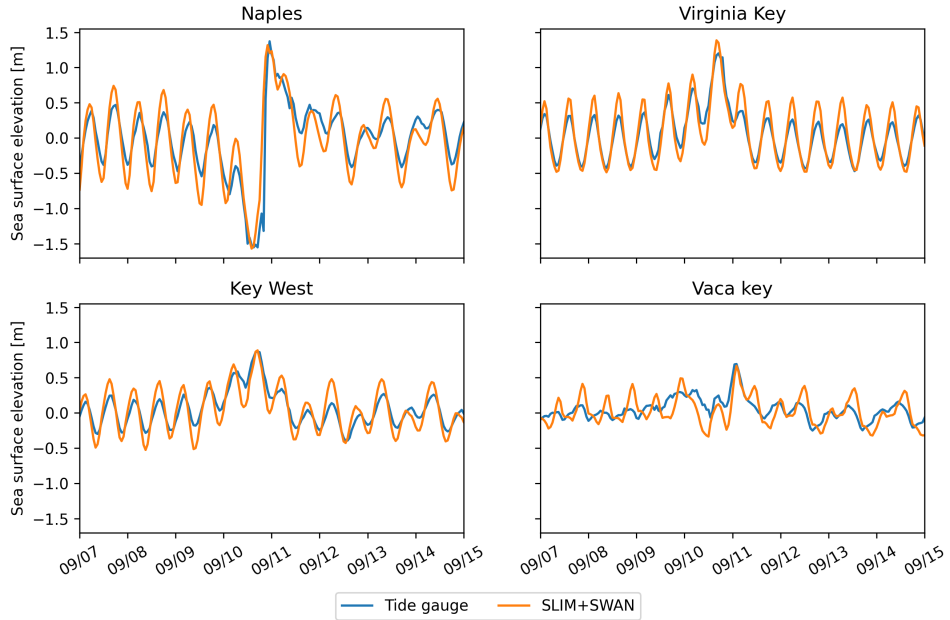


Fig. 4: Comparison of modelled sea surface elevation with all 4 tide gauge measurements (see Fig. 1B for their location). Timing and amplitudes of the storm surges are well reproduced by the model

correlation analysis of Kundu (1976) to compare modelled and observed current velocity vectors. Correlation coefficients (ρ) between simulated and observed depth-averaged currents were 0.84, 0.74 and 0.73 at the C10, C12 and C13 locations, respectively. Average veering angles were computed as well and were below 12° , as in (Liu et al., 2020). However, in our case, no clear tendency regarding modelled current behavior compared to observations was observed. As expected from a depth-averaged model, the best fit with observations is obtained at the shallowest mooring C10, located on the 25m isobath, with an average veering angle of 6° .

The simulated significant wave height agrees well with observations on the WFS, where errors on the peak value do not exceed 5% (Fig. fig:waves). On the East Florida Shelf, errors are slightly larger and reach 20%. Although the model outputs agree well with observations, a lag in significant wave height is observed for all 4 buoys. Moreover, the peak in significant wave height tends to be underestimated at buoys 41113 and 41114, located on the East Florida Shelf. Other wave parameters were better reproduced by the model on the WFS as well (see buoy 42036 in Fig. 6). This good fit on the WFS is not

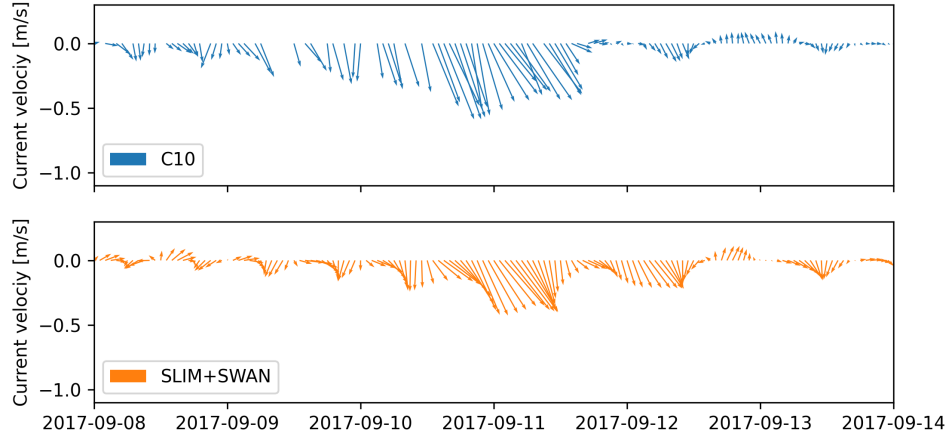


Fig. 5: Comparison of modelled current velocity with observed velocity at mooring C10 (see Fig. 1B for its location). Modelled current velocities agree well with observations, with a correlation coefficient of 0.83 and an average veering angle of 6° .

surprising as the parameters used for wind energy input and whitecapping dissipation were based on the calibration performed by Siadatmousavi et al. (2011) on the Northern Gulf of Mexico. Wind-induced wave growth might therefore be underestimated on the eastern shelf. Consequently, incident wave do not receive enough energy to grow after breaking on the bank boundary, leading to an underestimation of the significant wave height at the location of the buoys. Nonetheless, as this study focused on the wave produced by Irma, that made landfall on the western coasts of Florida, the use of parameterizations calibrated for the Gulf of Mexico seems reasonable.

3.2 Impact of waves on currents and transport

We evaluated the impact of wave-current interactions on modelled currents during the passage of Irma in the Lower Keys, between Sept. 7 and 13, 2017. First, we computed the maximum difference between currents modelled by SLIM and SLIM+SWAN during this period (Fig. 7A). The largest differences in current speed were observed over the reefs, on the shelf break and around islands. They can locally reach 1 m/s, with the coupled model SLIM+SWAN yielding the largest amplitudes. The regions where the differences are the largest experience the largest wave-induced stress τ_{wave} (7B), as wave

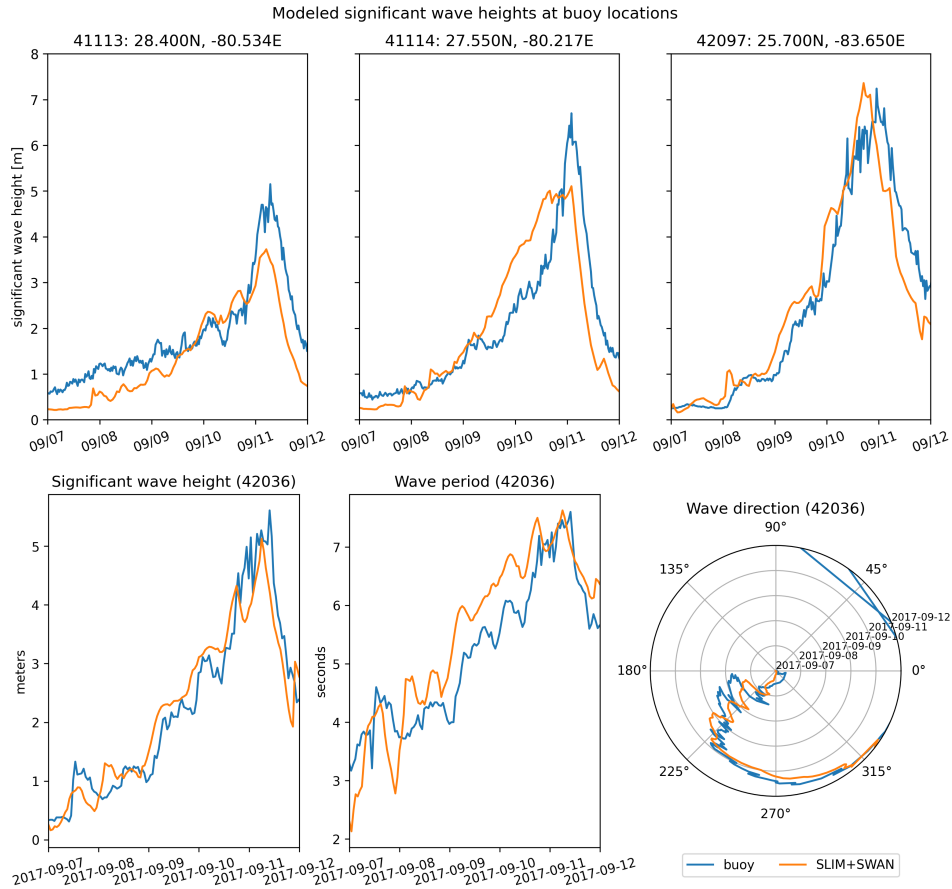


Fig. 6: Comparison of modelled wave parameters with observation at the 4 buoys location (locations shown in Fig. 1B). Modelled significant wave height agrees well with field measurement. As model parameters were calibrated for the Northern Gulf of Mexico, observations are better reproduced at buoys located on the WFS, as illustrated for buoy 42036

325 breaking and wave slowing down over rough seabed induce variations of the
326 wave radiation stress (Longuet-Higgins and Stewart, 1964). Wave-induced
327 differences in current speed were amplified by the action of the wind stress
328 τ_{wind} (Fig. 7C). Wind speeds were larger in the front right quadrant of the
329 hurricane (Zedler et al., 2009), yielding larger differences on the right-hand
330 side of the storm trajectory. This is especially clear in the area between
331 the Florida Keys and the Everglades, where relatively small values of τ_{wave}
332 nonetheless produce current speed differences of up to 0.5 m/s because of
333 the wind stress.

334 To quantify the impact of these differences in the velocity fields, we compared
335 the trajectories of passive particles advected by the uncoupled SLIM and
336 coupled SLIM+SWAN currents during the passage of Irma in the Lower
337 Keys (Fig. 8). Particles were released on the inner and outer shelves in
338 the areas highlighted by red and blue circles in Fig. 8A on 7 September
339 and then tracked until 15 September. These areas were constructed using
340 backtracking methods (Dobbelaeere et al., 2020a) to ensure that the release
341 particles would intersect the path of Irma during its passage in the Florida
342 Keys. We first defined two 25km^2 circular regions on the trajectory of
343 the hurricane (see red and blue circles in Fig. 8A). Particles within these
344 two regions were then tracked backward in time using uncoupled SLIM
345 currents from the exact time of the passage of the hurricane until the 7th of
346 September. Their positions at the end of the backward simulation (see red
347 and blue particle clouds in Fig. 8) corresponds to the initial condition of the
348 forward transport simulations described below.

349 We compared the trajectories of particles originating from these regions and
350 advected forward in time by different sets of currents: (i) uncoupled SLIM
351 currents alone; (ii) coupled SLIM+SWAN currents; (iii) SLIM currents with the
352 addition of the depth-averaged Stokes drift computed by the coupled wave
353 model (Stokes_C); (iv) SLIM+SWAN currents with Stokes_C; and (v) SLIM
354 currents with the depth-averaged Stokes drift computed by the uncoupled
355 wave model (Stokes_U). Particles trajectories are compared by computing
356 the distances between the centers of mass of the particle clouds through
357 time. Here are our main observations (*this needs to be improved, feedback
358 is welcome!*) :

- 359 • The impact of wave-current interactions is most important during the

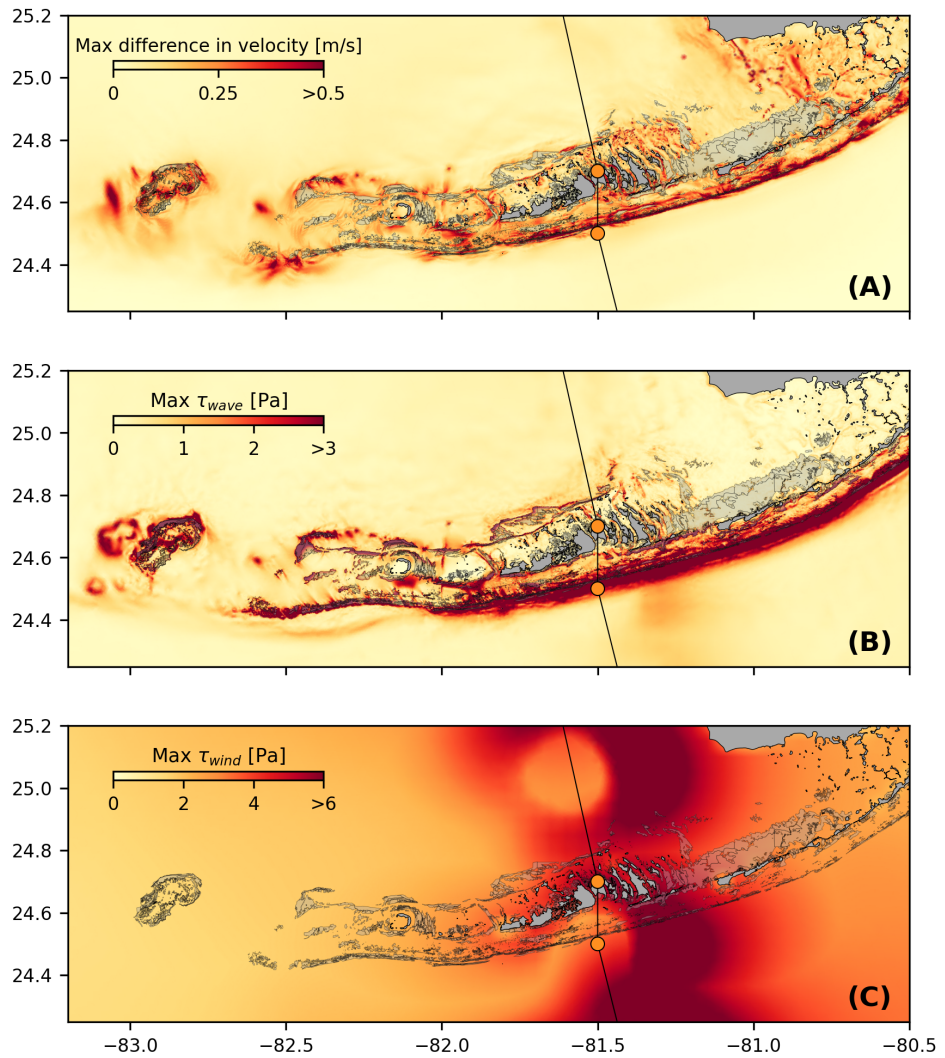


Fig. 7: Maximum difference between SLIM and SLIM+SWAN currents (A) during the passage of Irma in the Lower Florida Keys, along with the maximum wave radiation stress gradient τ_{wave} (B) and wind stress τ_{wind} (C) generated by the hurricane. Wave-induced stress yields difference larger than 0.5 m/s in current velocities. These wave-induced differences in currents were amplified by the action of the asymmetric wind profile of Irma, with larger differences occurring on the right of the storm trajectory

360 passage of the hurricane but negligible during the rest of the simulated
361 period. This is clear when comparing the clouds of particles advected
362 by SLIM and SLIM+SWAN on the outer shelf. The distance between
363 the centers of mass reaches 5 km during the passage of Irma but
364 tends to zero during the rest of the simulated period.

- 365 • The impact of the Stokes drift is larger than the impact of the wave-
366 current interactions on the inner shelf. The difference between the cen-
367 ters of mass does not exceed about 1 km for SLIM vs SLIM+SWAN but
368 reaches about 5 km for SLIM vs SLIM+Stokes_C and SLIM+SWAN+Stokes_C.
369 On the outer shelf, the currents are more intense and the impact the
370 wave-current coupling during the passage of the hurricane is suffi-
371 cient to generate a difference between the two clouds of particles that
372 keeps on increasing after the passage of the hurricane. The impact of
373 the Stokes drift remains however larger than the impact of the wave-
374 current coupling. This difference between the inner and outer shelf
375 can be explained by the sheltering of the inner shelf due to reefs and
376 islands as well as wave breaking on the shelf break. The inner shelf
377 hence experiences weaker waves and weaker currents, and hence
378 also weaker and more localised transport.
- 399 • On the inner shelf, the distance between the centers of mass of the
400 particle clouds stabilizes after the passage of the hurricane while this
401 distance keeps increasing during a couple of days after the passage
402 of the hurricane on the outer shelf under the action of the Stokes drift.
403 This shows the strong impact of wave-induced transport in the open
404 ocean.
- 425 • Impact of Stokes drift and wave-current interactions weaker on the
426 inner shelf. Max. distance of about 5 km between the centers of mass
427 of the clouds of particles compared to 30km on the outer shelves
- 448 • The fact that SLIM+Stokes_C vs. SLIM+Stokes_U keeps increasing on
449 the outer shelf after the passage of the hurricane shows the impact of
450 the strong current velocities of the FC on the modelled Stokes drift
- 472 • Nonetheless, the differences between the coupled and uncoupled
473 Stokes drifts remains relatively small with a maximum value of 2 km

393 between the centers of mass of the simulated particle clouds. Furthermore,
394 as SLIM vs SLIM+SWAN+Stokes and SLIM vs. SLIM+Stokes_C
395 show similar values on the inner shelf, this suggests that the combina-
396 tion of currents and Stokes drifts produces sufficiently accurate results
397 on sheltered shallow areas such as the WFS. However, neglecting
398 the wave-current interactions leads to differences of up to 5 km in
399 modelled particle trajectories on the outer shelf.

400 **4 Discussion and conclusions**

401 Impact of waves on coral connectivity

402 Ability of wave model to correctly capture gradient in significant wave height
403 due to current-waves interactions under tropical cyclones depends on:

- 404 • Broad perspective \Rightarrow not limited to FL
- 405 • Mention search and rescue
- 406 • However, ignoring waves in storm conditions could result in significant
407 inaccuracies in modelled trajectories, as illustrated in the case of
408 release region 2 in Fig. 8
- 409 • Spatial (10km \rightarrow 5km) and spectral (36 dir. \rightarrow 48 dir.) resolution
410 (Hegermiller et al., 2019)
- 411 • Directional spreading of incident waves (Villas Bôas et al., 2020)

412 **Conflict of Interest Statement**

413 The authors declare that the research was conducted in the absence of any
414 commercial or financial relationships that could be construed as a potential
415 conflict of interest.

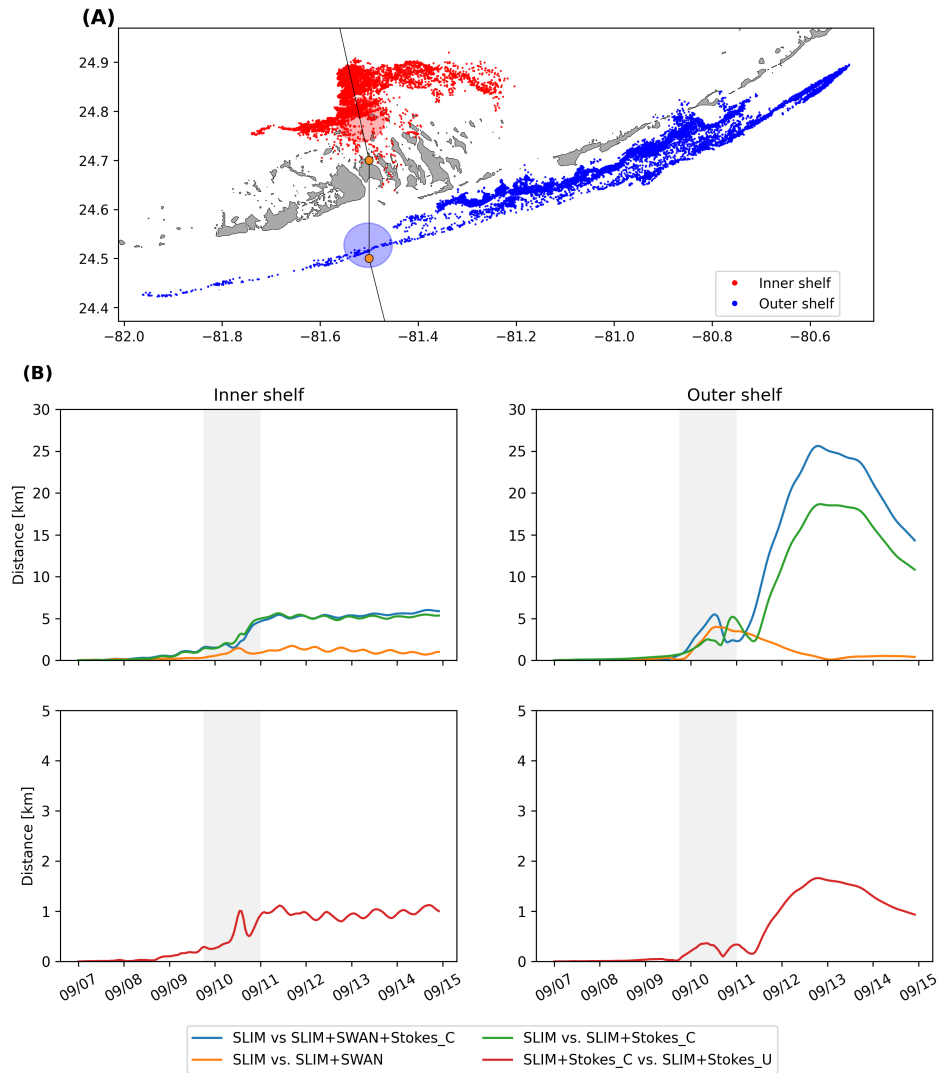


Fig. 8: A: Release regions of the passive particles on the inner and outer shelves (red and blue clouds) obtained by backtracking particles released in the red and blue circular areas during the passage of Irma (add a black border to the circles to better see them). **B:** Difference between the centers of mass of the particle clouds released from the regions highlighted in **A** and advected by different combinations of coupled and uncoupled velocity fields.

⁴¹⁶ **Author Contributions**

⁴¹⁷ **Funding**

⁴¹⁸ **Acknowledgments**

⁴¹⁹ Computational resources were provided by the Consortium des Équipements
⁴²⁰ de Calcul Intensif (CÉCI), funded by the F.R.S.-FNRS under Grant No. 2.5020.11.
⁴²¹ Thomas Dobbelaere is a PhD student supported by the Fund for Research
⁴²² training in Industry and Agriculture (FRIA/FNRS).

⁴²³ **Supplementary Material**

⁴²⁴ The Supplementary Material for this article is attached to the submitted
⁴²⁵ document.

⁴²⁶ **References**

- ⁴²⁷ Bever, A. J. and MacWilliams, M. L. (2013). Simulating sediment transport
⁴²⁸ processes in San Pablo Bay using coupled hydrodynamic, wave, and
⁴²⁹ sediment transport models. *Marine Geology*, 345:235–253.
- ⁴³⁰ Booij, N., Ris, R. C., and Holthuijsen, L. H. (1999). A third-generation wave
⁴³¹ model for coastal regions: 1. Model description and validation. *Journal*
⁴³² *of geophysical research: Oceans*, 104(C4):7649–7666.
- ⁴³³ Chassignet, E. P., Hurlbert, H. E., Smedstad, O. M., Halliwell, G. R., Hogan,
⁴³⁴ P. J., Wallcraft, A. J., Baraille, R., and Bleck, R. (2007). The HYCOM
⁴³⁵ (hybrid coordinate ocean model) data assimilative system. *Journal of*
⁴³⁶ *Marine Systems*, 65(1-4):60–83.
- ⁴³⁷ Chen, C., Huang, H., Beardsley, R. C., Liu, H., Xu, Q., and Cowles, G. (2007).
⁴³⁸ A finite volume numerical approach for coastal ocean circulation studies:
⁴³⁹ Comparisons with finite difference models. *Journal of Geophysical*
⁴⁴⁰ *Research: Oceans*, 112(C3).

- 441 Craik, A. D. and Leibovich, S. (1976). A rational model for Langmuir circula-
442 tions. *Journal of Fluid Mechanics*, 73(3):401–426.
- 443 Dietrich, J., Bunya, S., Westerink, J., Ebersole, B., Smith, J., Atkinson,
444 J., Jensen, R., Resio, D., Luettich, R., Dawson, C., et al. (2010). A
445 high-resolution coupled riverine flow, tide, wind, wind wave, and storm
446 surge model for southern Louisiana and Mississippi. part ii: Synoptic
447 description and analysis of hurricanes Katrina and Rita. *Monthly Weather
448 Review*, 138(2):378–404.
- 449 Dietrich, J., Westerink, J., Kennedy, A., Smith, J., Jensen, R., Zijlema, M.,
450 Holthuijsen, L., Dawson, C., Luettich, R., Powell, M., et al. (2011).
451 Hurricane Gustav (2008) waves and storm surge: Hindcast, synoptic
452 analysis, and validation in southern Louisiana. *Monthly Weather Review*,
453 139(8):2488–2522.
- 454 Dobbelaere, T., Muller, E., Gramer, L., Holstein, D., and Hanert, E. (2020a).
455 Report on the potential origin of the SCTLD in the Florida Reef Tract.
456 Available online at: [https://floridadep.gov/rcp/coral/documents/
457 report-potential-origin-sctld-florida-reef-tract](https://floridadep.gov/rcp/coral/documents/report-potential-origin-sctld-florida-reef-tract).
- 458 Dobbelaere, T., Muller, E. M., Gramer, L. J., Holstein, D. M., and Hanert, E.
459 (2020b). Coupled epidemic-hydrodynamic modeling to understand the
460 spread of a deadly coral disease in Florida. *Frontiers in Marine Science*,
461 7:1016.
- 462 Donelan, M., Haus, B., Reul, N., Plant, W., Stiassnie, M., Gruber, H., Brown,
463 O., and Saltzman, E. (2004). On the limiting aerodynamic roughness of
464 the ocean in very strong winds. *Geophysical Research Letters*, 31(18).
- 465 Drivdal, M., Broström, G., and Christensen, K. (2014). Wave-induced mixing
466 and transport of buoyant particles: application to the Statfjord a oil spill.
467 *Ocean Science*, 10(6):977–991.
- 468 Figueiredo, J., Baird, A. H., and Connolly, S. R. (2013). Synthesizing larval
469 competence dynamics and reef-scale retention reveals a high potential
470 for self-recruitment in corals. *Ecology*, 94(3):650–659.
- 471 Frys, C., Saint-Amand, A., Le Hénaff, M., Figueiredo, J., Kuba, A., Walker, B.,
472 Lambrechts, J., Vallaeys, V., Vincent, D., and Hanert, E. (2020). Fine-

- 473 scale coral connectivity pathways in the Florida Reef Tract: implications
474 for conservation and restoration. *Frontiers in Marine Science*, 7:312.
- 475 Garcia-Pineda, O., Androulidakis, Y., Le Hénaff, M., Kourafalou, V., Hole,
476 L. R., Kang, H., Staples, G., Ramirez, E., and DiPinto, L. (2020). Mea-
477 suring oil residence time with GPS-drifters, satellites, and Unmanned
478 Aerial Systems (UAS). *Marine pollution bulletin*, 150:110644.
- 479 Geuzaine, C. and Remacle, J.-F. (2009). Gmsh: A 3-d finite element mesh
480 generator with built-in pre-and post-processing facilities. *International*
481 *journal for numerical methods in engineering*, 79(11):1309–1331.
- 482 Harper, B., Kepert, J., and Ginger, J. (2010). *Guidelines for converting*
483 *between various wind averaging periods in tropical cyclone conditions*.
484 Citeseer.
- 485 Hegermiller, C. A., Warner, J. C., Olabarrieta, M., and Sherwood, C. R.
486 (2019). Wave–current interaction between Hurricane Matthew wave
487 fields and the Gulf Stream. *Journal of Physical Oceanography*,
488 49(11):2883–2900.
- 489 Hoefel, F. and Elgar, S. (2003). Wave-induced sediment transport and
490 sandbar migration. *Science*, 299(5614):1885–1887.
- 491 Hoffmeister, J. and Multer, H. (1968). Geology and origin of the Florida Keys.
492 *Geological Society of America Bulletin*, 79(11):1487–1502.
- 493 Holthuijsen, L. H., Powell, M. D., and Pietrzak, J. D. (2012). Wind and waves
494 in extreme hurricanes. *Journal of Geophysical Research: Oceans*,
495 117(C9).
- 496 Janssen, P. A. (1991). Quasi-linear theory of wind-wave generation applied
497 to wave forecasting. *Journal of physical oceanography*, 21(11):1631–
498 1642.
- 499 Johns, W. E. and Schott, F. (1987). Meandering and transport variations
500 of the Florida Current. *Journal of physical oceanography*, 17(8):1128–
501 1147.
- 502 Knaff, J. A., Sampson, C. R., and Musgrave, K. D. (2018). Statistical tropi-
503 cal cyclone wind radii prediction using climatology and persistence:

- 504 Updates for the western North Pacific. *Weather and Forecasting*,
505 33(4):1093–1098.
- 506 Knutson, T. R., McBride, J. L., Chan, J., Emanuel, K., Holland, G., Landsea,
507 C., Held, I., Kossin, J. P., Srivastava, A., and Sugi, M. (2010). Tropical
508 cyclones and climate change. *Nature geoscience*, 3(3):157–163.
- 509 Komen, G., Hasselmann, S., and Hasselmann, K. (1984). On the exis-
510 tence of a fully developed wind-sea spectrum. *Journal of physical*
511 *oceanography*, 14(8):1271–1285.
- 512 Kourafalou, V. H. and Kang, H. (2012). Florida Current meandering and
513 evolution of cyclonic eddies along the Florida Keys Reef Tract: Are they
514 interconnected? *Journal of Geophysical Research: Oceans*, 117(C5).
- 515 Kundu, P. K. (1976). Ekman veering observed near the ocean bottom.
516 *Journal of Physical Oceanography*, 6(2):238–242.
- 517 Landsea, C. W. and Franklin, J. L. (2013). Atlantic hurricane database un-
518 certainty and presentation of a new database format. *Monthly Weather*
519 *Review*, 141(10):3576–3592.
- 520 Langmuir, I. (1938). Surface motion of water induced by wind. *Science*,
521 87(2250):119–123.
- 522 Lee, T. N., Leaman, K., Williams, E., Berger, T., and Atkinson, L. (1995).
523 Florida Current meanders and gyre formation in the southern Straits
524 of Florida. *Journal of Geophysical Research: Oceans*, 100(C5):8607–
525 8620.
- 526 Lee, T. N. and Mayer, D. A. (1977). Low-frequency current variability and
527 spin-off eddies along the shelf off southeast Florida. *Collected Reprints*,
528 1(1):344.
- 529 Lee, T. N. and Smith, N. (2002). Volume transport variability through the
530 Florida Keys tidal channels. *Continental Shelf Research*, 22(9):1361–
531 1377.
- 532 Lee, T. N. and Williams, E. (1988). Wind-forced transport fluctuations of the
533 Florida Current. *Journal of Physical Oceanography*, 18(7):937–946.

- 534 Li, Z. and Johns, B. (1998). A three-dimensional numerical model of surface
535 waves in the surf zone and longshore current generation over a plane
536 beach. *Estuarine, Coastal and Shelf Science*, 47(4):395–413.
- 537 Lidz, B. H. and Shinn, E. A. (1991). Paleoshorelines, reefs, and a rising sea:
538 South florida, usa. *Journal of Coastal Research*, pages 203–229.
- 539 Lin, N. and Chavas, D. (2012). On hurricane parametric wind and appli-
540 cations in storm surge modeling. *Journal of Geophysical Research: Atmospheres*, 117(D9).
- 542 Liu, Y. and Weisberg, R. H. (2012). Seasonal variability on the West Florida
543 shelf. *Progress in Oceanography*, 104:80–98.
- 544 Liu, Y., Weisberg, R. H., and Zheng, L. (2020). Impacts of hurricane Irma
545 on the circulation and transport in Florida Bay and the Charlotte Harbor
546 estuary. *Estuaries and Coasts*, 43(5):1194–1216.
- 547 Liubartseva, S., Coppini, G., Lecci, R., and Clementi, E. (2018). Tracking
548 plastics in the Mediterranean: 2D Lagrangian model. *Marine pollution
549 bulletin*, 129(1):151–162.
- 550 Longuet-Higgins, M. S. (1970). Longshore currents generated by obliquely
551 incident sea waves. *Journal of geophysical research*, 75(33):6778–
552 6789.
- 553 Longuet-Higgins, M. S. and Stewart, R. (1964). Radiation stresses in water
554 waves; a physical discussion, with applications. In *Deep sea research
555 and oceanographic abstracts*, volume 11, pages 529–562. Elsevier.
- 556 Madsen, O. S., Poon, Y.-K., and Gruber, H. C. (1989). Spectral wave
557 attenuation by bottom friction: Theory. In *Coastal Engineering 1988*,
558 pages 492–504.
- 559 Malmstadt, J., Scheitlin, K., and Elsner, J. (2009). Florida hurricanes and
560 damage costs. *southeastern geographer*, 49(2):108–131.
- 561 Marsooli, R., Lin, N., Emanuel, K., and Feng, K. (2019). Climate change
562 exacerbates hurricane flood hazards along US Atlantic and Gulf Coasts
563 in spatially varying patterns. *Nature communications*, 10(1):1–9.

- 564 McWilliams, J. C. and Sullivan, P. P. (2000). Vertical mixing by Langmuir
565 circulations. *Spill Science & Technology Bulletin*, 6(3-4):225–237.
- 566 Mei, C. C. (1989). *The applied dynamics of ocean surface waves*, volume 1.
567 World scientific.
- 568 Moon, I.-J., Ginis, I., Hara, T., and Thomas, B. (2007). A physics-based
569 parameterization of air–sea momentum flux at high wind speeds and
570 its impact on hurricane intensity predictions. *Monthly weather review*,
571 135(8):2869–2878.
- 572 Pinelli, J.-P., Roueche, D., Kijewski-Correa, T., Plaz, F., Prevatt, D., Zisis,
573 I., Elawady, A., Haan, F., Pei, S., Gurley, K., et al. (2018). Overview
574 of damage observed in regional construction during the passage of
575 Hurricane Irma over the State of Florida. In *Forensic Engineering 2018:*
576 *Forging Forensic Frontiers*, pages 1028–1038. American Society of
577 Civil Engineers Reston, VA.
- 578 Powell, M. D., Houston, S. H., Amat, L. R., and Morisseau-Leroy, N. (1998).
579 The HRD real-time hurricane wind analysis system. *Journal of Wind
580 Engineering and Industrial Aerodynamics*, 77:53–64.
- 581 Powell, M. D., Vickery, P. J., and Reinhold, T. A. (2003). Reduced drag coeffi-
582 cient for high wind speeds in tropical cyclones. *Nature*, 422(6929):279–
583 283.
- 584 Röhrs, J., Christensen, K. H., Hole, L. R., Broström, G., Drivdal, M., and
585 Sundby, S. (2012). Observation-based evaluation of surface wave
586 effects on currents and trajectory forecasts. *Ocean Dynamics*, 62(10–
587 12):1519–1533.
- 588 Schott, F. A., Lee, T. N., and Zantopp, R. (1988). Variability of structure and
589 transport of the Florida Current in the period range of days to seasonal.
590 *Journal of Physical Oceanography*, 18(9):1209–1230.
- 591 Shinn, E. A. (1988). The geology of the Florida Keys. *Oceanus*, 31(1):46–53.
- 592 Siadatmousavi, S. M., Jose, F., and Stone, G. (2011). Evaluation of two WAM
593 white capping parameterizations using parallel unstructured SWAN
594 with application to the Northern Gulf of Mexico, USA. *Applied Ocean
595 Research*, 33(1):23–30.

- 596 Sikirić, M. D., Roland, A., Janeković, I., Tomazić, I., and Kuzmić, M. (2013).
597 Coupling of the Regional Ocean Modeling System (roms) and Wind
598 Wave Model. *Ocean Modelling*, 72:59–73.
- 599 Smith, N. P. (1982). Response of Florida Atlantic shelf waters to hurricane
600 David. *Journal of Geophysical Research: Oceans*, 87(C3):2007–2016.
- 601 Stokes, G. G. (1880). On the theory of oscillatory waves. *Transactions of*
602 *the Cambridge philosophical society*.
- 603 Tolman, H. L. et al. (2009). User manual and system documentation of
604 WAVEWATCH III TM version 3.14. *Technical note, MMAB Contribution*,
605 276:220.
- 606 Van Den Bremer, T. and Breivik, Ø. (2018). Stokes drift. *Philosophical Trans-*
607 *actions of the Royal Society A: Mathematical, Physical and Engineering*
608 *Sciences*, 376(2111):20170104.
- 609 Villas Bôas, A. B., Cornuelle, B. D., Mazloff, M. R., Gille, S. T., and Arduin,
610 F. (2020). Wave–current interactions at meso-and submesoscales:
611 Insights from idealized numerical simulations. *Journal of Physical*
612 *Oceanography*, 50(12):3483–3500.
- 613 Weisberg, R., Liu, Y., and Mayer, D. (2009). Mean circulation on the west
614 Florida continental shelf observed with long-term moorings. *Geophys.*
615 *Res. Lett*, 36:L19610.
- 616 Weisberg, R. H. and Zheng, L. (2006). Hurricane storm surge simulations
617 for Tampa Bay. *Estuaries and Coasts*, 29(6):899–913.
- 618 Wu, L., Chen, C., Guo, P., Shi, M., Qi, J., and Ge, J. (2011). A FVCOM-
619 based unstructured grid wave, current, sediment transport model, I.
620 Model description and validation. *Journal of Ocean University of China*,
621 10(1):1–8.
- 622 Xian, S., Feng, K., Lin, N., Marsooli, R., Chavas, D., Chen, J., and Hatzikyri-
623 akou, A. (2018). Brief communication: Rapid assessment of damaged
624 residential buildings in the Florida Keys after Hurricane Irma. *Natural*
625 *Hazards and Earth System Sciences*, 18(7):2041–2045.

626 Zedler, S., Niiler, P., Stammer, D., Terrill, E., and Morzel, J. (2009). Ocean's
627 response to Hurricane Frances and its implications for drag coefficient
628 parameterization at high wind speeds. *Journal of Geophysical Re-*
629 *search: Oceans*, 114(C4).

630 Zhang, C., Durgan, S. D., and Lagomasino, D. (2019). Modeling risk of man-
631 groves to tropical cyclones: A case study of Hurricane Irma. *Estuarine,*
632 *Coastal and Shelf Science*, 224:108–116.